# **DELINEATION OF MINOR-SPACE PHOTOCONDUCTIVE** DIPOLE ANTENNA FOR TERAHERTZ VISUALIZATION

## <sup>1</sup>Prakash Chandra Meshram, <sup>2</sup>Ajay Kumar Jain, <sup>3</sup>Ashok Kumar Sagar

Research Scholar, Department of Electronics and Communication Engineering, LNCT University, Bhopal, India<sup>1</sup> Research Scholar, Department of Civil Engineering, LNCT University, Bhopal, India<sup>2</sup> Research Scholar, Department of Civil Engineering, LNCT University, Bhopal, India<sup>3</sup>

Abstract: Due to its unique properties, the THZ regime of electromagnetic spectrum is rich in new possibilities for a variety of applications, including wireless communication, imaging, non-destructive testing, security scans, and process control. The unique features of THZ waves are its nonionized radiation, superior resolution than microwaves, unique spectral absorption, and ability to pass through dielectrics. Spectroscopy with high spectral resolution at frequencies in the THZ region is an influential analytical instrument for examining the structure and energy levels of molecules and atoms. While THZ spectroscopy may be used to recognize explosive and illegal drugs, THZ radiation is covered as it can be transmitted quickly by materials such as plastics, paper products, luggage, clothing, and other non- conductive materials. It uses simple synthesis techniques to determine the physical parameters of PCDA with FSS. Thin overload is also used under the dipole antenna to improve antenna radiation efficiency, which also contributes to the overall efficiency of PCDA. This means that the antenna can withstand high voltages. Additionally, bending illumination imaging is required to design antennas with wavelengths. As a result, the antenna design is compact. Additionally, silicon lenses in built antenna configurations allow focusing on beams focused in the desired direction. Additionally, the proposed PCDA using silicon lenses improves the antenna output. This can be useful for THZ acquisition and image applications such as: Using the proposed simple PCDA and thin super-straight and silicon lenses, we achieved a direct 10.7 dBi of 91.59% at both the E and H levels and radiation efficiency.

Frequency Keywords: Selective Surface (FSS), Photoconductive Dipole Antennas (PCDA), Terahertz (THZ)

#### INTRODUCTION

A portion of the electromagnetic spectrum between the optical domain and the microwave regime is known as the THZ gap [1]. The well-developed technology of the microwave regime and the optical domain of the electromagnetic spectrum, basic research, advanced technology development, new initiatives in the THZ band are very limited and relatively unexplored, so it has been called in the past. As shown in Figure 1, electronics (mmillimeter waves) and photonics (infrared waves) are divided into THZ bands where semiconductor electronics

and optical technologies find applications. Reliable, compact, temperature sensitive and efficient performance sources and cap non-availability were the most important obstacles to the popularity of the THZ band in the electromagnetic spectrum. Over the past 20 years, significant advances in technology have been made, with the development of solid-state modes and quantum cascade lasers, laser base THZ domestic spectroscopy, and microelectron production of planar antennas leveling the pathways of imaging technology in the THZ frequency band.

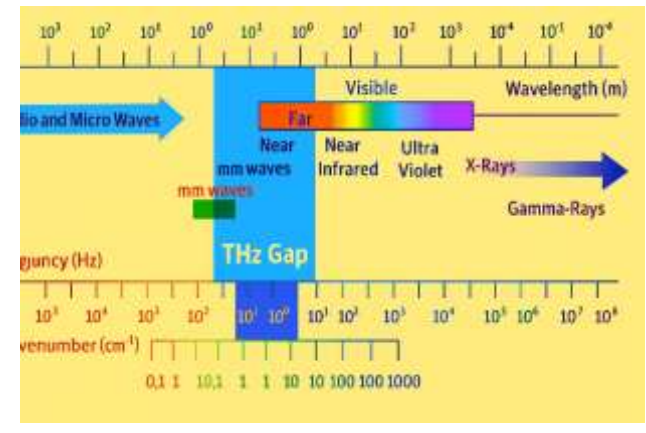


Figure 1: THZ region

Furthermore, with the advent of ER+-doped FEMTO-seconds fiber lasers, it has been replaced by sapphire lasers for expensive systems: THZ systems made of titanium [2]. Due to many other technical tasks in the field of semiconductor physics and technology, many researchers [3] are currently examining the use of the licensing-one THZ band of electromagnetic spectrum for various potential applications. Recently, in the case of the electromagnetic spectrum of biological imaging [4], nondestructive testing [5], security scan [6, 7], and process control [8] have been introduced to the next-generation [9] wireless communication systems. In the domain of the electromagnetic spectrum, there is multiple interactions between electromagnetic waves and matter, leading to several biological, chemical, molecular, and physical structures to show unique spectral fingerprints, in addition to rotational modes with specific frequencies of the band. Furthermore, the high absorption of THZ radiation from oxygen molecules containing polar liquids such as water is the main limitation of atmospheric waves on the long route [10].

### II. THZ WAVE PROPERTIES

The THz area has been of interest since the 1920s, but substantial research on this spectrum has only been conducted in the last three decades. The region has gained quick attention due to its extraordinary wave characteristics and endless usage possibilities in the THz frequency range. The THz region has mid-band features

from both the IR and MW millimetre (mm) regions since it is confined between them. THz radiation possesses several distinctive properties that contribute to its unique characteristics and make it valuable for various applications. Here are some key properties of THz radiation [11]:

**Non-ionizing:** The non-ionizing nature of THz waves is a pivotal aspect that distinguishes them from higher-energy electromagnetic radiations, such as X-rays and gamma rays. THz waves, falling within the non-ionizing region of the electromagnetic spectrum, lack the energy required to ionize atoms or molecules by dislodging electrons.

**Distinctive spectral fingerprints:** THz waves interact with molecular vibrations and rotations, providing unique spectral fingerprints for different materials. This allows for precise identification and characterization of substances based on their THz absorption or reflection patterns. Transmission properties will give more precise values of Refractive index and absorption coefficient.

Non-destructive testing: THz radiation is commonly used in non-destructive testing of materials. It enables the inspection of structures and materials without causing damage, making it useful for quality control and structural integrity assessments.

High-resolution imaging: THz waves enable highresolution imaging, making them valuable for imaging applications in fields such as medicine, security, and materials science. They can reveal details not easily captured by other imaging techniques.

Penetration through non-conductive materials: THz radiation can penetrate through this penetration property arises from the relatively long wavelengths of THz waves, allowing them to navigate through the materials that are typically opaque to visible light. In practical terms, this feature has significant implications for fields such as security screening, where THz waves can be employed to detect concealed objects without the need for harmful ionizing radiation.

Communication potential: THz frequencies offer the potential for high-speed communication due to their wide bandwidth. Researchers are exploring communication for applications like ultra-fast wireless data transfer. Its ability to accommodate ultra-high data speeds, up to terabits per second (Tbps), is one of the THz band's most important advantages. The increasing need video streaming, and more is being met by this, which is orders of magnitude higher than the peak rates now offered by 6G.

Sensitivity to water: THz radiation is highly sensitive to water content, making it effective for imaging and sensing applications in biological tissues. This property is exploited in medical imaging for detecting abnormalities and diseases.

**Low atmospheric absorption**: THz radiation experiences relatively low absorption by atmospheric gases, particularly in dry air. This characteristic allows for the observation of THz signals over longer distances.

#### III. ANALYSIS ANTENNA OF FSS

This makes everyone related to their merit and adjacent [12]. Furthermore, FSS structures can be interpreted as complementary filters. Equivalent circuit models are very well accepted under the analytical procedures for analyzing FSS. This is due to the simplicity of comparable parameters of FSS captured leaves on the dielectric. Similar to the proposed antenna structure, the FSS structure was used together with the photographic cartilage dipole antenna to increase the reinforcement and guidelines. Therefore, FSS is used as a bandpass-spatial filter. Figure 2 shows the unit cell design of the FSS bandpass and the S-parameter reaction of the FSS unit cell. Metal elements represent inductive screens leading to overall reflections, and the openings in the metal increase for overall transmission [13]. In addition to physical characteristics like the unit cell FSS's periodicity (p), slot length (d), and slot width (s), the gap between the two slots (g) also affects the analysis and design of bandpass FSS. The parameters of square bandpass FSS are determined by the synthesis process of unit Zel-FSS, which is explained. Therefore, the same synthetic technique was presented in designing bandpass Quadratform-FSS with more specific uses of this technique.

In the proposed antenna design, the use of a dielectric substrate with FSS provides physical integrity to the FSS structure, so that dielectric contaminated FSS-Bandpass is further used rather than using prominent use at will. Additionally, it also provides stable reflectance and transmission characteristics, and allows for the basic resonance frequency to be altered [14]. The unit cell structure of the bandpass FSS is shown in Figure 2(a).

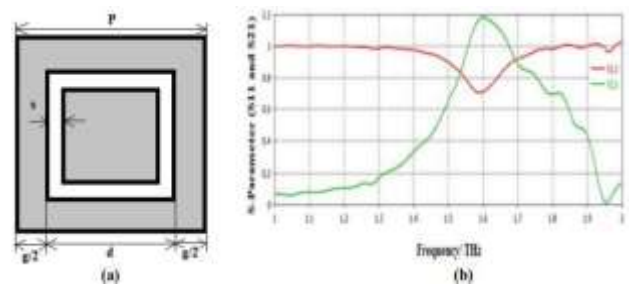


Figure 2: The single square loop FSS

It is made of aluminum for metal paving with conductivity  $\sigma$ =3.5×107 s/m and is arranged at  $\epsilon_R$ =1.05

via a building of relative plates via a dielectric substrate. Furthermore, the use of dielectric materials changes the performance of FSS structures [15]. This occurs because the above-mentioned characteristic impedance and FSS structures are changed by the presence of dielectric materials.

The thickness of the related dielectric substrate must last to avoid evanescent waves spreading into the normal FSS structure. As the thickness of the FSS and  $\lambda_0$  dielectric substrates is  $\lambda_0/20$ , which is the wavelength of the open space, avoidance becomes a wave, affecting the performance of the periodic structure.

The physical parameters of the FSS unit cell were computed at 1.5 THZ in order to examine the theory presented in the preceding subsection of the FSS bandpass unit cell. The FSS bandpass unit cell's physical properties are computed for typical incident waves, as seen in Figure  $2 (\Theta = 0^{\circ})$ , as it is assumed that only THZ radiation from the normal indication was created, as the temporary solder in the HFSS microwave studio is supported by the normal incidence of electromagnetic waves on the structure. The relationship between the periodicity (p) and slit length (d) of unit cells in FSS with normal incidence, i.e. [p(1+sin  $0^{\circ}$ )]  $<\lambda$  and P $<\lambda$ . The designed PCA has an operating frequency of 1.5.5. The open space wavelength is 250 µm. The periodicity of the FSS unit cell is maintained below 250 µm. The substrate size of the designed PCA is 300 x 300 µm<sup>2</sup> and the size of the substrate of the FSS with the designed antenna with the overall configuration using FSS -Bandpass -unitcell - Car is also assumed to be 300 x 300  $\mu$ m<sup>2</sup>. Periodicity of different sizes of the array as p = 160 for 2x2 FSS, p = 130 for 3x3 fss, and p = 110 for 4x4 fss. For various values of p (about 160, roughly 130, and 110 µm), the values of m are computed at 0.75, 0.5, and 0.375 in order to meet. Should the value of M be set to a different  $S/\lambda$  value, the slit length value is calculated and in Tables 1, 2, 3 for three types of array setups using PCDA ( $2\times2$ ) FS,  $(3\times3)$  FSS and  $(4\times4)$  and  $(4\times4)$  and  $(4\times4)$  and  $(4\times4)$ and

 $(4\times4)$  and  $(2\times2)$  FSS. The number of gaps between the for various values of p (about 160, roughly 130, and 110

μm), the values of m are computed at 0.75, 0.5, and 0.375 in order to meet. Should the value of M be set to a

different S/λ value,

Table 1: FSS band pass unit cell physical parameters for 2×2 FSS array.

s/λ	s(um) for λ=250 μm	P(µm)	D(µm)	G=P-d (μm)	g/2 (µm)
0.01	3	160	53.47	106.53	53.26
0.02	5	160	58.72	101.28	50.64
0.03	7	160	63.46	96.54	48.27

0.04	9	160	68.88	91.12	45.56

Table II: FSS band pass unit cell physical parameters for 3×3 FSS array.

Ī	s/λ	s(um) for	P(µm)	D(µm)	G=P-d	g/2	
		λ=250			(µm)	(µm)	
		μm					
ſ	0.01	3	130	57.22	72.78	36.39	
ſ	0.02	5	130	62.42	67.58	33.79	
ſ	0.03	7	130	67.12	62.88	31.44	
	0.04	9	130	72.34	57.66	28.83	

Table III: FSS band pass unit cell physical parameters for 4×4 FSS array.

s/λ	s(um) for	P(µm)	D(µm)	G=P-d	g/2
	λ=250			(µm)	(µm)
	μm				
0.01	3	110	63.12	46.88	23.44
0.02	5	110	66.44	43.56	21.78
0.03	7	110	69.88	40.12	20.06
0.04	9	110	72.12	37.38	18.94

#### IV. RESULTS

This section provides a full analysis of the proposed aerial, which was conducted with the use of an HFSS electromagnetic simulator. The change in |S11| for a single port aerial is shown in Fig. 3 for three distinct scenarios: (i) without ceramic, (ii) with cylindrical ceramic, and (iii) with ring ceramic. It demonstrates that ceramic is in charge of the entire operational range of the proposed aerial. Because the radiator's effective permittivity is lower in the case of ring-shaped ceramic, a larger impedance bandwidth is seen.

The |S11| curve shows two resonant peaks. Fig. 3 shows the E-field at 2.55 THz and 3.1 THz to identify the peaks' respective responsibilities. Two basic hybrid orthogonal modes (HEM\_11 $\delta$ ^x and HEM\_11 $\delta$ ^y) are created at 2.55 THz and 3.1 THz, as shown in Fig. 3 [17]. This resonance frequency can also be verified using the algebraic equation that follows [18]:

$$f_{r, \text{HEM}_{118}} = \frac{_{6.324c}}{_{2\pi D}\sqrt{\epsilon_{eFF}+2}} \{0.27 + 0.36 \left(\frac{^{D}}{_{4H_{eFF}}}\right) +$$

$$0.02 \left(\frac{D}{4H_{oFF}}\right)^{2} \} \tag{1}$$

$$\varepsilon_{\text{eff}} = \frac{H_{eFF}}{H + H_{S}} \tag{2}$$

ε<sub>ring</sub> ε<sub>SiO2</sub>

$$H_{\text{eff}} = H + H_{\text{S}} \tag{3}$$

$$\varepsilon_{\text{ring}} = \frac{\varepsilon_{\text{Si}} \times V_{\text{weramiw}} + \varepsilon_{\text{air}} \times V_{\text{air}}}{V_{\text{weramiw}} + V_{\text{air}}}$$
(4)

$$V_{ceramic} = V_{Si} - V_{air}$$
 (5)

The resonant frequency, 2.75 THz, is discovered after entering all the values in the aforementioned equations; this number is near to the simulated result.

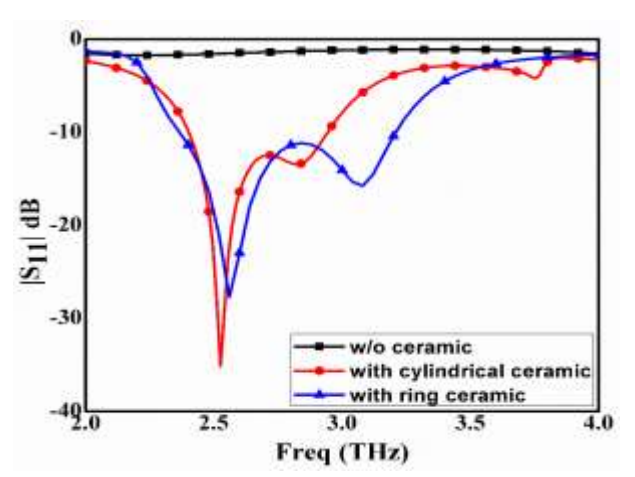


Figure 3: Change in  $|S_{11}|$  for single port in case of with and without ceramic

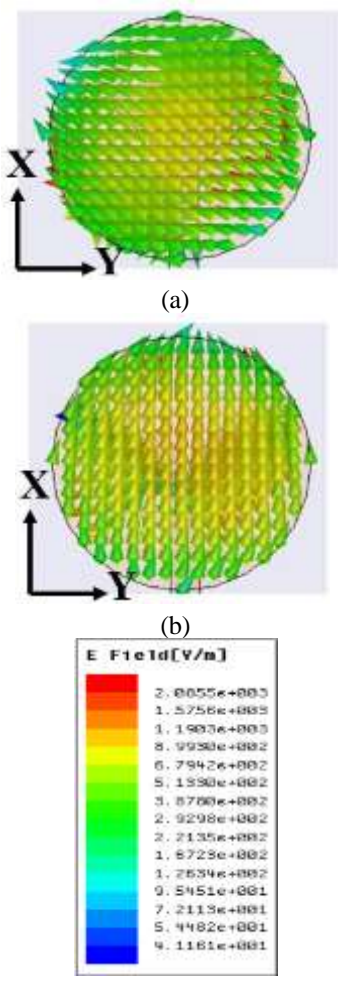


Figure 4 E-field rotation on Si-ceramic (a) 2.55 THz (b) 3.1 THz

Fig. 5 shows the |S11| curve following several slot shape variations. For this aim, three examples are selected: (i) ceramic fed by a circular aperture; (ii) ceramic fed by an equal-arm fan blade; and (iii) ceramic fed by an unequal-

arm fan blade. The axial ratio change is shown in Fig. 6 using the identical scenarios as previously indicated. Figure 6 shows that less than 3 dB of AR is delivered by the fan blade (unequal arm). The fan blade's uneven arms cause a 900 phase shift by providing varying travel delays to orthogonal modes. The development of CP waves requires this.

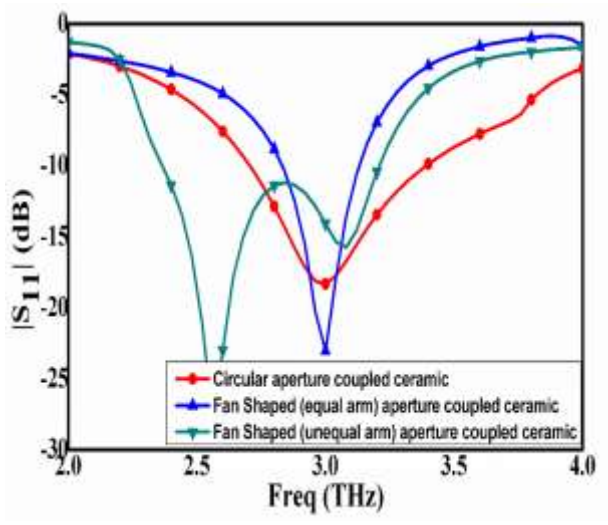


Figure 5:  $|S_{11}|$  fluctuation with different aperture shape modifications

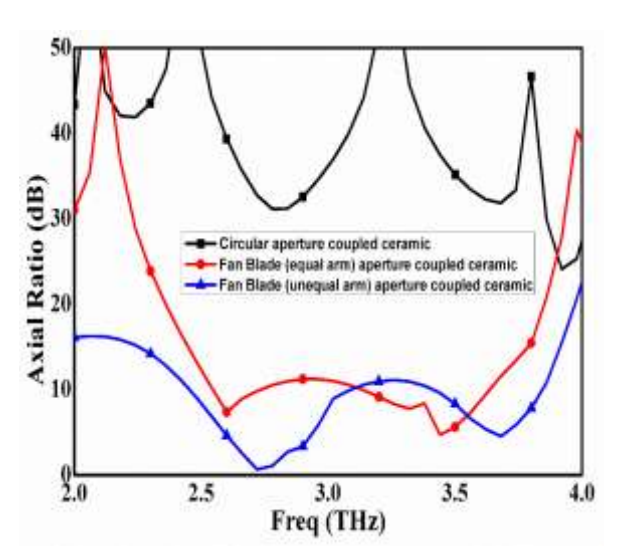


Figure 6: Axial ratio fluctuation with different aperture shape modifications

The silicon ceramic is made adjustable by covering it with a layer of graphene. By varying the chemical potential ( $\mu$ c), graphene's intra-band conductivity may be altered. This can be confirmed using the following mathematical equation [10]:

$$\sigma_{intra}(\omega,\mu_c,\Gamma,T) = -j \frac{e^{2K}T}{\pi\hbar^2(\omega-j2\Gamma)} \left(\frac{\mu_c}{c} + 2ln\left(e^{-\frac{\mu_c}{K_BT}} + \frac{1}{2}ln\left(e^{-\frac{\mu_c}{K_BT}} + \frac{$$

The variables KB, T,  $\mu c$ , and  $\Gamma$  stand for the temperature, chemical potential, scattering rate, and Boltzmann

constant, respectively, in the equation above. By altering the graphene layer's electrostatic potential, chemical potential may be modified. The single-port aerial's  $|S_{11}|$ curve is revealed in Fig. 7. It shows that when the chemical potential ( $\mu$ c) value rises, the  $|S_{11}|$  curve moves to higher frequencies. The shift in axial ratio with variations in graphene's chemical potential is seen in Fig.

8. As the chemical potential ( $\mu c$ ) value increases, it is clear from Fig. 8 that the 3-dB axial ratio band changes to higher frequencies. As a result, frequency flexibility of the planned THz radiator is demonstrated.

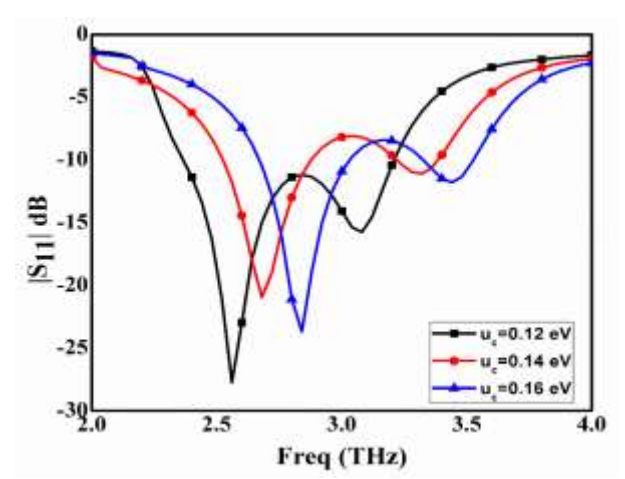


Figure 7: Change in  $|S_{11}|$  with varying in chemical potential of graphene

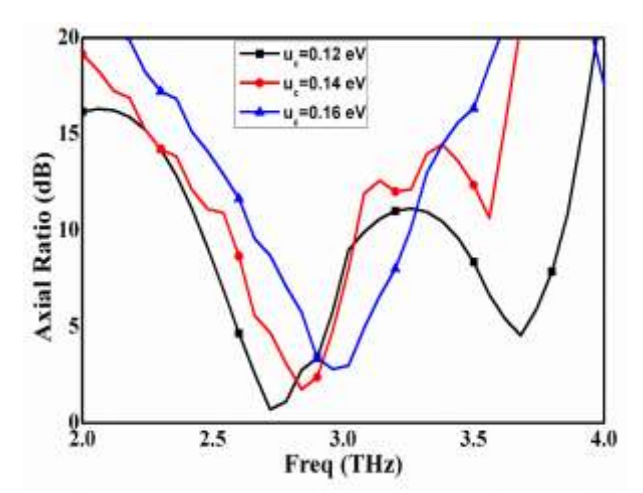


Figure 8: Change in axial ratio with varying in chemical potential of graphene

#### V. CONCLUSION

The benefits are greatly improved and the directivity of photorate dipol antennas using bandpass-FSS as superstruts at Terahertz frequency for the present invention and imaging are presented. Furthermore, the effects of unit cell cycles of FSS are examined in the resonance state of shows that the required transmission tape of the THZ signal is achieved by variation in the value of  $S/\lambda$  using FSS-Superstrat using photo-ring dipol antennas. The proposed photorant with a 4-FSS bandpass structure is used on the top and bottom of the antenna. This indicates a significant improvement in yield loss, profit, directness, and performance values for frontal

relationships of the field where the object is at its distance considered in the focus. However, the performance of FSS is heavily influenced by a variety of other factors, including ohmic loss, surface roughness, ladder dispersion, and skin depth that stands out.

#### REFERENCES

- Kononenko, T.V.; Ashikkalieva, K.K.; Kononenko, V.V.; Zavedeev, E.V.; Dezhkina, M.A.; Komlenok, M.S.; Ashkinazi, E.E.; Bukin, V.V.; Konov, V.I. Diamond Photoconductive Antenna for Terahertz Generation Equipped with Buried Graphite Electrodes. Photonics 2023, 10, 75.
- Kononenko, V.V.; Komlenok, M.S.; Chizhov, P.A.; Bukin, V.V.; Bulgakova, V.V.; Khomich, A.A.; Bolshakov, A.P.; Konov, V.I.; Garnov, S.V. Efficiency of photoconductive terahertz generation in nitrogen-doped diamonds. Photonics 2022, 9, 18.
- Chai, X.; Ropagnol, A.; Ovchinnikov, O.; Chefonov, A.; Ushakov, C.; Garcia-Rosas, C.M.; Isgandarov, E.; Agranat, M.; Ozaki, T.; Savel'ev, A. Observation of crossover from intraband to interband nonlinear terahertz optics. Opt. Lett. 2018, 43, 5463.
- Ma, W.; Li, C.; Wang, Z.; Li, L.; Wang, S.; Sun, C. Application of Terahertz Time-Domain Spectroscopy in Characterizing Thin Metal Film-Substrate Structures. IEEE Trans. Terahertz Sci. Technol. 2020, 10, 593-598.
- Collier, C. M., Stirling, T. J., Hristovski, I. R., Krupa, J. D. A. & Holzman, J. F. Photoconductive terahertz generation from textured semiconductor materials. Sci. Rep. 6, 1-10 (2016).
- Yardimici, N. T., Yang, S. & Jarrahi, M. High Power Pulsed Terahertz Radiation from Large Area Plasmonic Photoconductive Emitters. In Infrared, Millimeter, and Terahertz waves (IRMMW-THz) 8-9 (2015).
- Yang, S., Hashemi, M. R., Berry, C. W. & Jarrahi, M. 7.5% Optical-to-Terahertz Conversion Efciency Photoconductive Emitters With Tree-dimensional Contact Plasmonic Electrodes. IEEE Trans. Terahertz Sci. Technol. 4, 1–7
- Bashirpour, M., Kolahdouz, M. & Neshat, M. Enhancement of optical absorption in LT-GaAs by double layer nanoplasmonic array in photoconductive antenna. Vacuum. 146, 430-436 (2017).
- Ghorbani, S. et al. Tin Film Tandem Nanoplasmonic Photoconductive Antenna for High Performance Terahertz Detection. Superlattices Microstruct. 120, 598-604 (2018).
- 10. Bashirpour, M., Ghorbani, S., Forouzmehr, M., Kolahdouz, M. R. & Neshat, M. Optical absorption enhancement in LTG-GaAs for efciency improvement of THz photoconductive antennas. In Millimeter-Wave and Terahertz Technologies (MMWaTT), 2016 Fourth International Conference on 14-16 (IEEE, 2016).
- 11. Park, S.-G. et al. Enhancement of terahertz pulse emission by optical nanoantenna. ACS Nano 6, 2026-2031 (2012).
- 12. Lepeshov, S. et al. Boosting the Terahertz Photoconductive Antenna Performance with Optimized Plasmonic Nanostructures. Sci. Rep. 8, 6624 (2017).
- 13. Akbar, F., Kolahdouz, M., Larimian, S., Radfar, B. & Radamson, H. H. Graphene synthesis, characterization and its applications in nanophotonics, nanoelectronics, and nanosensing. J. Mater. Sci. Mater. Electron. 26, 1-33 (2015).
- 14. Lepeshov, S., Gorodetsky, A., Krasnok, A., Rafailov, E. & Belov, P. Enhancement of terahertz photoconductive antenna operation by optical nanoantennas. Laser Photon. Rev. 20, 1-20 (2016).
- 15. Poursafar, J. et al. Ultrathin solar cells with Ag meta-material nanostructure for light absorption enhancement. Sol. Energy 166, 98-102 (2018).
- 16. Soleimanzadeh, R., Kolahdouz, M., Charsooghi, M. A., Kolahdouz, Z. & Zhang, K. Highly selective and responsive ultraviolet detection using an improved phototransistor. Appl. Phys. Lett. 106, 231102 (2015).
- 17. Karegar, F. et al. Light-Emitting n-ZnO Nanotube/n+-GaAs Heterostructures Processed at Low Temperatures. IEEE Photonics Technol. Lett. 27, 1430–1433 (2015)